

MICROSTRUCTURE AND TENSILE PROPERTIES OF HPDC Mg–RE ALLOYS WITH VARYING Y ADDITIONS

Lingyun Feng 

School of Mechanical Science and Engineering, Huazhong University of Science and Technology, Wuhan 430074, China
College of Mechanical and Electrical Engineering, Nanjing University of Aeronautics and Astronautics, Nanjing 210016, China

Brunel Centre for Advanced Solidification Technology (BCAST), Brunel University London, Uxbridge, Middlesex UB8 3PH, UK

Xixi Dong

College of Mechanical and Electrical Engineering, Nanjing University of Aeronautics and Astronautics, Nanjing 210016, China

Qing Cai and Shouxun Ji

Brunel Centre for Advanced Solidification Technology (BCAST), Brunel University London, Uxbridge, Middlesex UB8 3PH, UK

Copyright © 2024 The Author(s)
<https://doi.org/10.1007/s40962-024-01266-z>

Abstract

High-pressure die-casting Mg–2.6RE–xY (EW) alloys with Y contents between 0 and 3% (in wt%) were investigated for their microstructure and tensile properties. In the Y-containing alloy, the intermetallic phases at the grain boundaries consisted of skeletal Mg₁₂RE phase, bulk Mg₂₄Y₅ phase and irregular Mg₃Y phase, while {011} twins were observed in the Mg₁₂RE phase. The yield strength was improved by Y addition at both room temperature and high temperatures. Compared with Y-free alloy, the yield strength of 3% Y alloy increased from 143.1 to 174.8 MPa and improved by 22.2% at room temperature, while it was increased from 72.2 to 104.6 MPa and enhanced by 44.9% at 300 °C. The area fraction of intermetallic phase increased dramatically from 14.5 to 18.4% with 3% Y

addition. Second phase strengthening was the major contributor to the yield strength increase at ambient temperature. The increment of the area fraction of the high-thermally stable Mg–RE intermetallic phases with Y addition contributed to the consequent improvement in yield strength at high temperatures. At ambient temperature, the mechanism for the fracture of EW alloys was a ductile and quasi-cleavage fracture blend.

Keywords: high-pressure die-casting, microstructures, tensile properties, strengthening mechanism, Mg–RE alloys

Supplementary Information The online version contains supplementary material available at <https://doi.org/10.1007/s40962-024-01266-z>.

This paper is an invited submission to IJMC selected from presentations at the Light Metals Technology Conference (LMT2023) held July 10 to 12, 2023, in Melbourne, Australia, based upon the original presentation.

Received: 11 November 2023 / Accepted: 10 January 2024

Published online: 19 February 2024

Introduction

Magnesium (Mg) alloys have been widely used in automotive, aircraft, telecommunications, and biomedical industries.^{1,2} Magnesium alloys are considered an adequate replacement for steel and aluminium alloys, leading to adequate energy savings and weight reduction.^{3,4} In consideration of the actual production efficiency and economic profit, the magnesium alloy compounds currently used are manufactured mainly with a high-pressure die-casting (HPDC) process.⁵ However, low–high-temperature (HT)

strength and insufficient heat resistance are still significant impediments for the scaling utilisation of HPDC Mg alloys. Therefore, research is urgently needed to enhance the HT tensile properties of HPDC Mg alloys.

Magnesium alloys are considerably improved through deformation hardening, alloying, grain refinement, and heat treatment.^{6–8} Alloying is the most effective and direct of these methods.^{1,6} The alloying with elements including Al, Si, Mn, alkaline earth, and rare earth (RE) on Mg alloys have been investigated extensively, generating the development of various Mg alloys.¹ Representative alloys include Mg–5Al–2Si (AS52, unless otherwise noted, all compositional references in the text are to wt%),⁹ Mg–5Al–3Ca–0.15Sr (AXJ530),¹⁰ Mg–5Al–3Ca–0.3Mn (AXM5303),¹¹ Mg–3.2Al–4.4La–0.5Nd,¹² Mg–4Al–4RE (AE44),¹³ Mg–3.5RE–1.5Gd–0.5Al,¹⁴ Mg–4.2Y–3.3RE–0.5Zr (WE43),¹⁵ and Mg–Gd–Y–Zn–Zr.¹⁶

The most common HPDC Mg alloys used are Mg–Al alloys, with classic Mg–Al alloys AZ91 and AM50/60.^{14,17} Due to the unstable Mg₁₇Al₁₂ phase at elevated temperatures, Mg–Al alloys are challenged to apply at higher working temperatures.¹⁷ RE elements have been reported to strengthen the tensile properties and castability of Mg alloys, so HPDC AE42 and AE44 alloys have been developed.^{13,17} In the AE series alloys, single additions of light RE elements or misch metals are reported to have decent performance in enhancing tensile properties.^{13,17} These light RE elements have low relative solid-solubility in the α -Mg and can consume Al to form Al–RE phases to inhibit the Mg₁₇Al₁₂ phase formation, thus improving the HT tensile properties along with the room temperature (RT) tensile properties.^{4,18} RE elements, including Gd and Y, are also investigated in Mg–Al-based alloys. Al₂Gd and Al₂Y phases formed during solidification are reported to act as heterogeneous nucleation sites to achieve grain refinement.¹⁹ However, the potential formation of the Mg₁₇Al₁₂ phase at HT makes the AE series alloys still hard to work above 200 °C.¹³ Research on Al-free HPDC Mg–RE alloys has been carried out to achieve good heat resistance, represented by the HP2+ and MEZ alloys.²⁰ The thermally stable Mg–RE intermetallic compounds in these alloys result in excellent strength and creep performance up to 200 °C.¹ However, higher RE content increases the risk of hot cracking.²¹ Moreover, the investigated alloying

elements in these HPDC Mg–RE alloys without Al addition are mostly limited to La, Ce, and Nd. In our previous study, the addition of the heavy RE element, Gd, to the Mg–2.6RE alloy was investigated, which led to various thermal stable Mg–RE phase formations to enhance the tensile properties at HT.^{22,23}

Yttrium, a Y group element with three valence electrons and high solubility, has been reported to strengthen Mg alloys.^{1,24,25} Due to the dense distribution of Mg₅(Gd,Y) and Mg₂₄(Gd,Y)₅ phases, adding Y can enhance the strength of aged Mg–10Gd–xY–0.4Zr significantly.²⁶ In the ZK60–1Y alloy, 1% Y addition improved mechanical properties with ternary I-phase and W-phase.²⁷ Although there have been few studies on Y-containing HPDC Mg–RE alloys,⁵ the function of Y on microstructure and both RT and HT tensile properties has not yet been determined.

This research aims to research the microstructure and tensile properties of HPDC Mg–2.6RE–xY ($x = 0–3$) (EW) alloys. The strengthening mechanism in the Y addition alloys was also discussed.

Experimental Methods

A resistance furnace and a steel crucible were utilised to melt the alloy. Pure magnesium was first added to the crucible for melting, followed by pure zinc and, subsequently, Mg–30% La, Mg–5%Mn, Mg–25%Ce and Mg–30%Y master alloys. The melting temperature was 720 °C. The deflagration-preventing protective gas was composed of a mixture of 0.5% SF₆ and N₂. The mushroom samples were cast to test composition with inductively coupled plasma (ICP).²⁰ Die casting was accomplished utilising FRECH 4500kN cold-chamber machine without vacuum, while the intensification pressure and injection speed were set at 320 bar and 4 m/s, separately. Before pouring the melt, the temperature of the molten alloy was controlled with the thermocouple. The mould for die casting was preheated before casting to 220 °C. The mould used for die casting can make 8 ASTM standard ϕ 6.35-mm round and 50-mm gauge length samples simultaneously²⁰ (Table 1).

The tensile tests complied with the RT tensile standard ASTM B557-15 and the HT tensile standard ASTM E8/

Table 1. Chemical Composition of Experimental EW Alloys Obtained by ICP

Alloy code	Alloy	La	Ce	Y	Zn	Mn	Mg
EW300	Mg1.6La1Ce–0Y	1.62	0.95	0.07	0.47	0.28	Bal.
EW305	Mg1.6La1Ce–0.5Y	1.58	0.94	0.42	0.49	0.27	Bal.
EW310	Mg1.6La1Ce–1Y	1.56	0.97	0.91	0.51	0.26	Bal.
EW315	Mg1.6La1Ce–1.5Y	1.61	0.99	1.44	0.48	0.27	Bal.
EW320	Mg1.6La1Ce–2Y	1.54	1.00	1.93	0.49	0.24	Bal.
EW330	Mg1.6La1Ce–3Y	1.58	0.98	2.91	0.46	0.31	Bal.

E8M-16, respectively. The Instron 5500, equipped with Bluehill software, served as apparatus for the tensile tests. In an electrical resistance furnace, HT tensile tests were conducted. Moreover, the test temperature was controlled by a temperature control box. A 50-mm pitch extensometer was used to gauge the elongation during the RT tensile test. For the HT tensile test, there was no extensometer. Tensile rates for the tests conducted at RT were 1 mm/min, and at HT were 0.0002/s. The average tensile properties with standard deviation were achieved through the tensile test of six samples.

For microstructure observation, the centre section of the sample bar was utilised. A backscattered electron (BSE) mode micrograph was presented with a ZEISS scanning electron microscope (SEM). After being mounted, ground, and polished with 320–4000 grit SiC papers, fumed colloidal silica suspension, and a medium polishing disc, samples were ready for SEM analysis. Transmission electron microscope (TEM) samples were ion polished with 3.0–5.0 kV and the corresponding 3°–5° angle. Thin ion-polished samples were used to capture images on a JEOL 2100F TEM device. The grain size and phase area fraction were calculated using ImageJ software. On a D8 instrument with 2θ range of 20° to 100° and DIFFRAC EVA software, X-ray diffraction (XRD) and analysis were performed. The ImageJ software was used to measure phase area fraction based on at least 10 SEM images and grain size distribution by using a linear intercept method.

Results

XRD Patterns

Figure 1 displays XRD patterns analysis results of HPDC EW300, EW305, EW310, EW315, EW320, and EW330 alloys. The XRD patterns indicated that the major detected

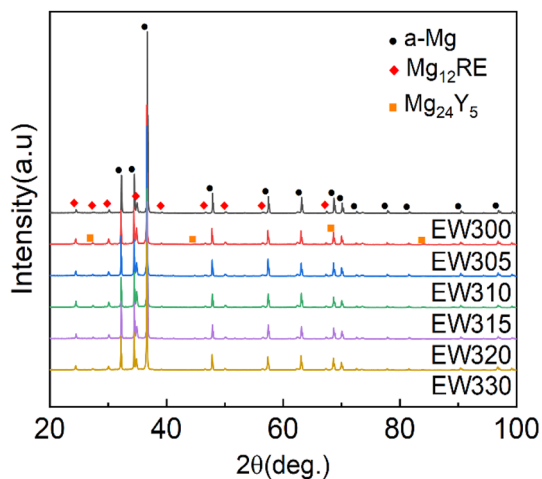


Figure 1. XRD patterns analysis results of HPDC EW300, EW305, EW310, EW315, EW320, and EW330 alloys.

phases were α -Mg and $Mg_{12}RE$. In addition to α -Mg and $Mg_{12}RE$, a minor peak of the $Mg_{24}Y_5$ phase can be detected in HPDC EW305, EW310, EW315, EW320, and EW330 alloys. It is essential to mention that small-sized or area-fraction phases are typically difficult for XRD to identify.

Comprehensive Microstructure

Figure 2a–f presents statistical grain size distribution results of the as-cast HPDC EW300, EW305, EW310, EW315, EW320, and EW330 alloys. The line scribing method revealed a mean grain size (d_{mean}) of 9.4 μm for EW300 alloy, with large grains reaching 33 μm . Furthermore, the d_{mean} decreased slightly with increasing Y addition, with an 8.3 μm d_{mean} for EW315 alloy. However, with further addition of Y, the d_{mean} of the alloys stabilised. The d_{mean} was 8.4 μm in EW330 alloy, with large grains measuring around 30 μm . Higher Y additions led to a smaller d_{mean} in the alloy, but the ensuing variations were not statistically significant. In addition, the fractions of intermetallic compounds at GBs for EW300, EW305, EW310, EW315, EW320, and EW330 alloys are depicted statistically in Figure 3. The fraction of intermetallic phase at the GBs grown steadily with increasing Y additions, but then levelled off at EW320 alloy.

Figure 4a–f depicts high-magnification BSE-SEM images of intermetallic compounds on GBs in HPDC EW300, EW305, EW310, EW315, EW320, and EW330 alloys. The dominant intermetallic phase in the EW300 alloy featured a skeleton-like morphology. Its morphology resembled the $Mg_{12}RE$ intermetallic phase, which had been previously reported.^{23,28} In addition, the dominant $Mg_{12}RE$ intermetallic phase gradually assumed a flaky morphology as the Y content increased. Two minor intermetallic phases with Y content were also formed as the continuous addition of Y, one was a more extensive blocky $Mg_{24}Y_5$ phase, and the other was a more minor irregular Mg_3Y intermetallic phase. Both Y-containing intermetallic phases can be observed in alloys above 0.5% Y additions.

Characterisation of Intermetallic Phase

Characterisation of $Mg_{12}RE$ Phase

Figure 5 displays the analysis of TEM images on the dominant $Mg_{12}RE$ intermetallic phase at GBs of HPDC EW330 alloy. Figure 5a displays a bright-field TEM (BF-TEM) micrograph of the GB in HPDC EW330 alloy, which reveals skeleton-like structure of the $Mg_{12}RE$ intermetallic phase. According to the EDX results in Supplementary Fig. S1 and Table S1, atomic ratios of Mg: (La, Ce, Y, Zn) indicated that dominant intermetallic phase at GBs was $Mg_{12}RE$, which corresponded with the XRD detected

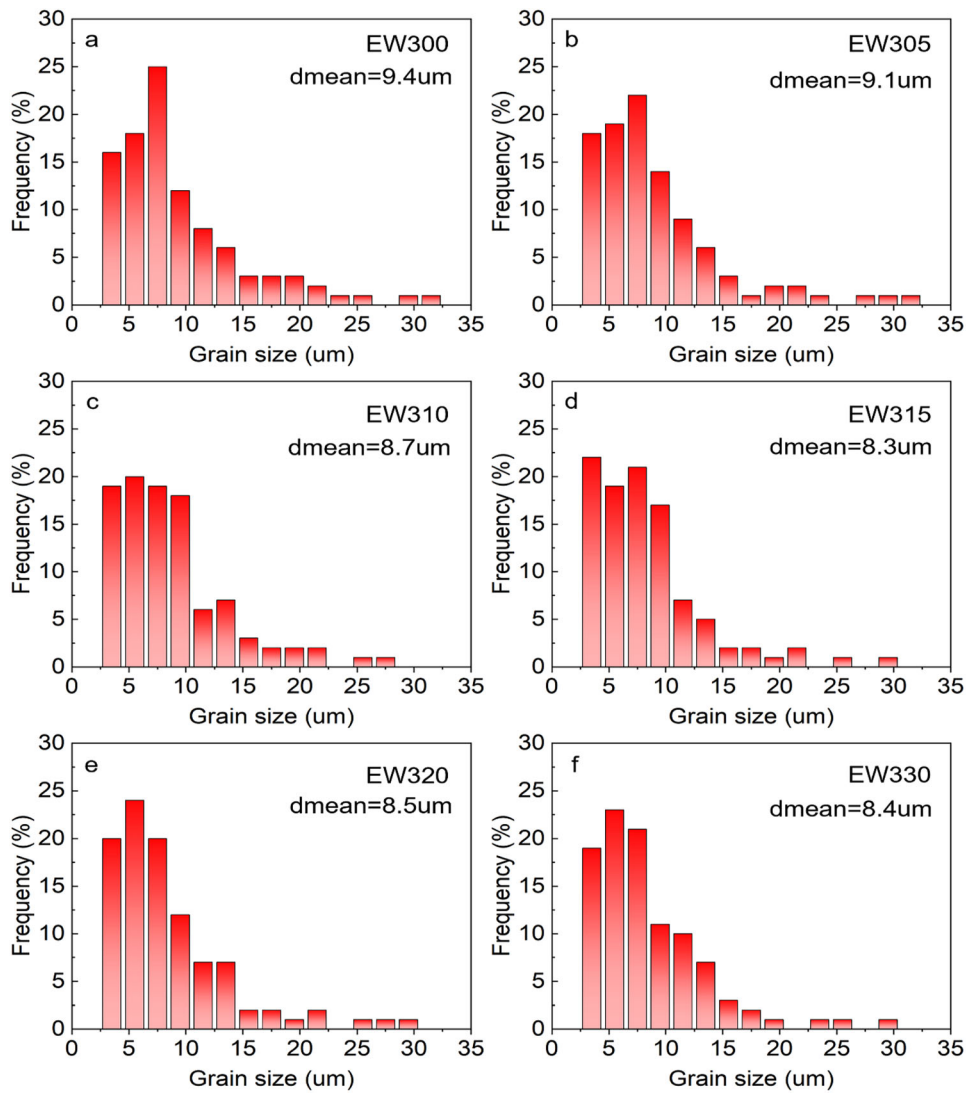


Figure 2. Grain size distribution result of α -Mg phase in HPDC (a) EW300, (b) EW305, (c) EW310, (d) EW315, (e) EW320, and (f) EW330 alloys. (g) Area fraction of intermetallic compounds in HPDC EW300, EW305, EW310, EW315, EW320, and EW330 alloys.

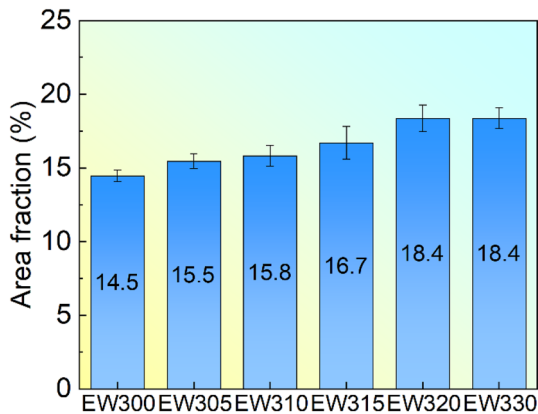


Figure 3. Area fraction of intermetallic compounds in HPDC EW300, EW305, EW310, EW315, EW320, and EW330 alloys.

results. The $Mg_{12}RE$ phase formation in Mg–La/Ce alloys was primarily attributed to the reduced nucleation barrier.²⁹ The selected area electron diffraction (SAED) analysis results in Figure 5b indicated that the dominant skeleton-like compound was $Mg_{12}RE$. In addition, the high-resolution TEM (HRTEM) micrograph and fast Fourier transfer (FFT) analysis result in Figure 5c further confirmed it. Additionally, the SAED analysis image in Figure 5b demonstrated the existence of {011} twins in $Mg_{12}RE$. Moreover, the HRTEM micrograph and corresponding FFT analysis results shown in Figure 5e, f further confirmed the existence of twins. Previous research on Mg–La/Ce–Gd and Mg–4Zn–2La–3Y alloys revealed the existence of {011} twins in the $Mg_{12}RE$ phase.^{22,30} It has been reported that the generation of twins in $Mg_{12}RE$ phase is majorly due to the segregation of Zn elements.³¹ The presence and content

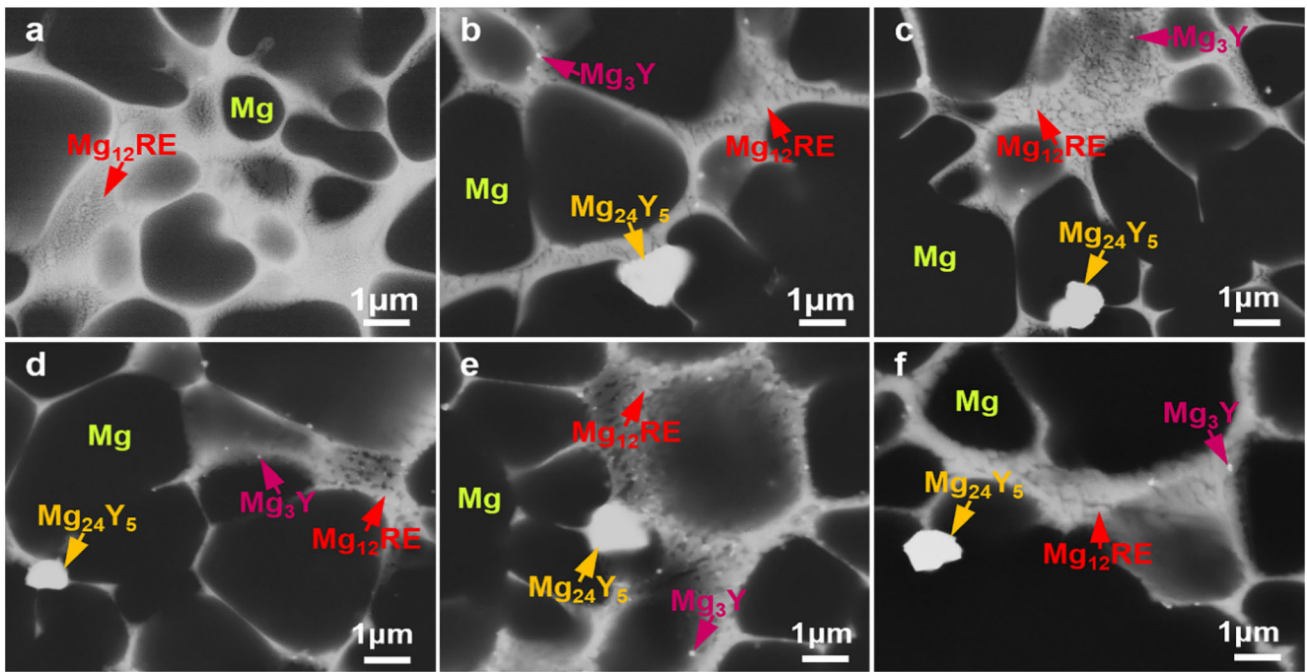


Figure 4. High-magnification BSE-SEM image of HPDC (a) EW300, (b) EW305, (c) EW310, (d) EW315, (e) EW320, and (f) EW330 alloys displaying intermetallic compounds at GBs.

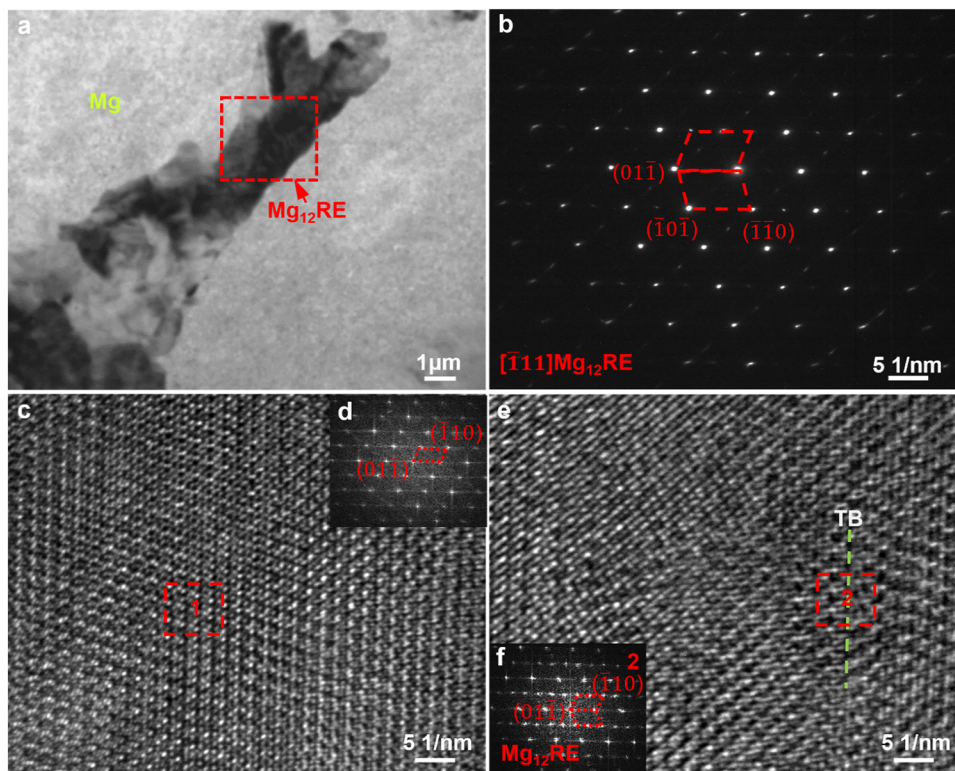


Figure 5. Micrographs of the dominant $Mg_{12}RE$ intermetallic phase at GBs in HPDC EW330 alloy. (a) BF-TEM micrograph of the GB; (b) SAED for the $Mg_{12}RE$ phase detected in $[111]$ zone axis; (c) and (e) HRTEM of $Mg_{12}RE$ phases; (d) and (f) the corresponding FFT for $Mg_{12}RE$ phases in (c) and (e), respectively.

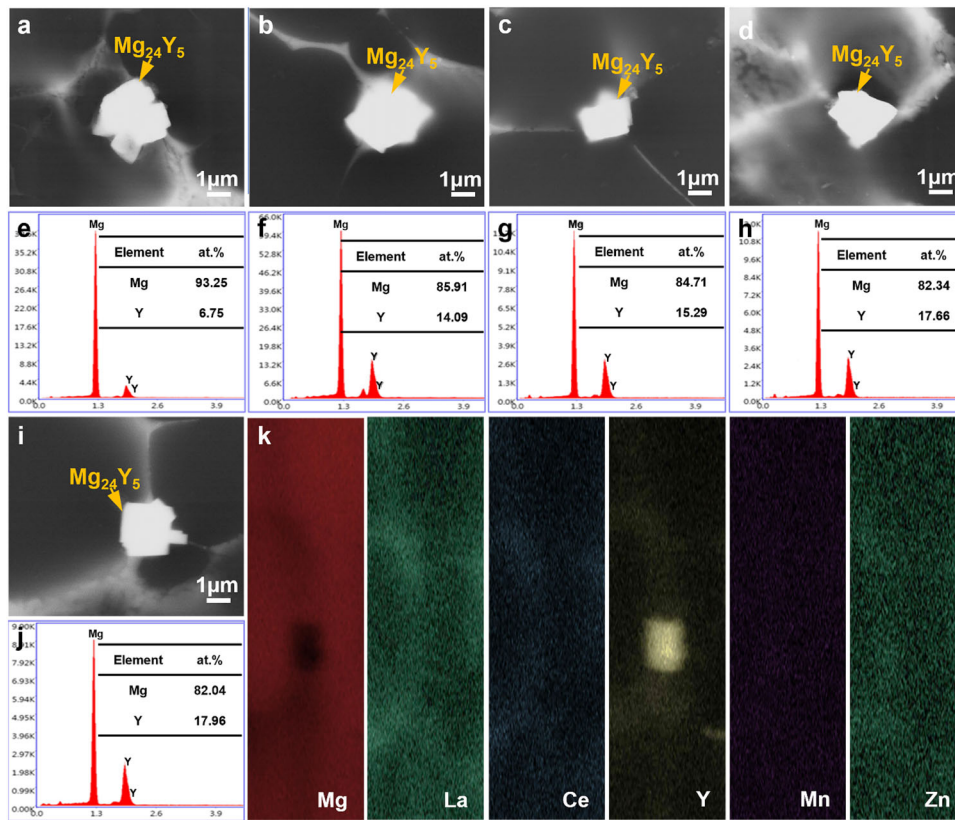


Figure 6. High-magnification BSE-SEM images and EDX-SEM spot scanning analysis results of the minor blocky $Mg_{24}Y_5$ phases at GBs of HPDC (a, b) EW305, (c, d) EW310, (e, f) EW315, (g, h) EW320, (i, j) EW330; (k) EDX-SEM mapping results of Mg, La, Ce, Y, Mn, and Zn in (i).

of Zn in $Mg_{12}RE$ are shown in Supplemental Table S1, which further supports the formation of twins in $Mg_{12}RE$.

Characterisation of $Mg_{24}Y_5$ Phase

Figure 6 depicts a detailed characterisation of the minor blocky $Mg_{24}Y_5$ phase in HPDC EW305, EW310, EW315, EW320, and EW330 alloys. Figure 6a, c, e, g, i shows the morphology of the $Mg_{24}Y_5$ phase. The corresponding energy-dispersive X-ray (EDX-SEM) spot scanning results shown in Figure 6b, d, f, h, j indicated that the minor blocky intermetallic compounds primarily consisted of Mg and Y, and the atomic ratio of Mg/Y decreased continuously with increasing Y addition, fluctuating between 5 and 6. According to the XRD patterns result and the corresponding scanning results in Figure 6b, d, f, h, j, the blocky intermetallic phases in the HPDC EW305, EW310, EW315, EW320, and EW330 alloys can be thought of as $Mg_{24}Y_5$. The segregation of element Y at GBs has been reported to contribute to the $Mg_{24}Y_5$ phase formation.³² In addition, the EDX-SEM mapping results in Figure 6k revealed that the minor $Mg_{24}Y_5$ phase was primarily enriched in Mg and Y, with no aggregation of other elements.

Characterisation of Mg_3Y Phase

Figure 7 displays a detailed analysis of the small irregular Mg_3Y minor intermetallic phases in HPDC EW330 alloy. The BF-TEM image in Figure 7a indicated that the small irregular intermetallic phases were dispersed in eutectic regions with a size of approximately 100–200 nm. The EDX-STEM results in Figure 7b indicated that two elements, Mg and Y, were predominantly present in the small irregular intermetallic phases and the contents of La, Ce, and Zn were relatively low, and the Mg/(La,Ce,Y,Zn) atomic ratio was lower than that in $Mg_{24}Y_5$, which was approximately 3. Furthermore, the EDX-STEM mapping result in Figure 7c–h showed no apparent aggregation of Zn, La, Ce, and Mn. Therefore, the small irregular intermetallic phase should be the Mg_3Y phase. Burapornpong et al.³³ suggested that the Mg_3Y phase, with a similar crystal structure to Mg_3La , would decompose into the $Mg_{24}Y_5$ phase and the Mg_2Y phase at 588 K. The presence of the minor Mg_3Y phase was attributable to the restriction of Y diffusion due to the high cooling rate of the HPDC.^{34,35} The thermal stability of Mg_3Y up to 588 K in the alloy indicated it could improve the tensile strength at 300 °C.

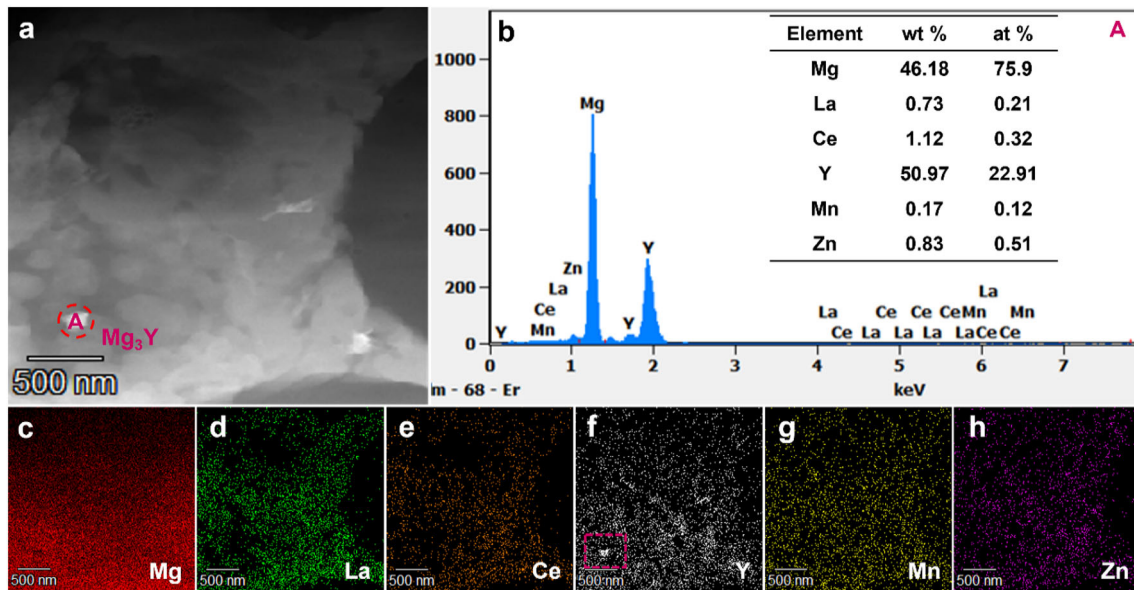


Figure 7. TEM micrograph and EDX-STEM analysis result of the minor irregular Mg_3Y intermetallic phase at GBs in HPDC EW330 alloy. (a) BF-TEM micrographs of the Mg_3Y phase; (b) EDX-STEM analysis result of Mg_3Y intermetallic phase in (a); (c–h) EDX-STEM mapping results of (c) Mg, (d) La, (e) Ce, (f) Y, (g) Mn, and (h) Zn in (a).

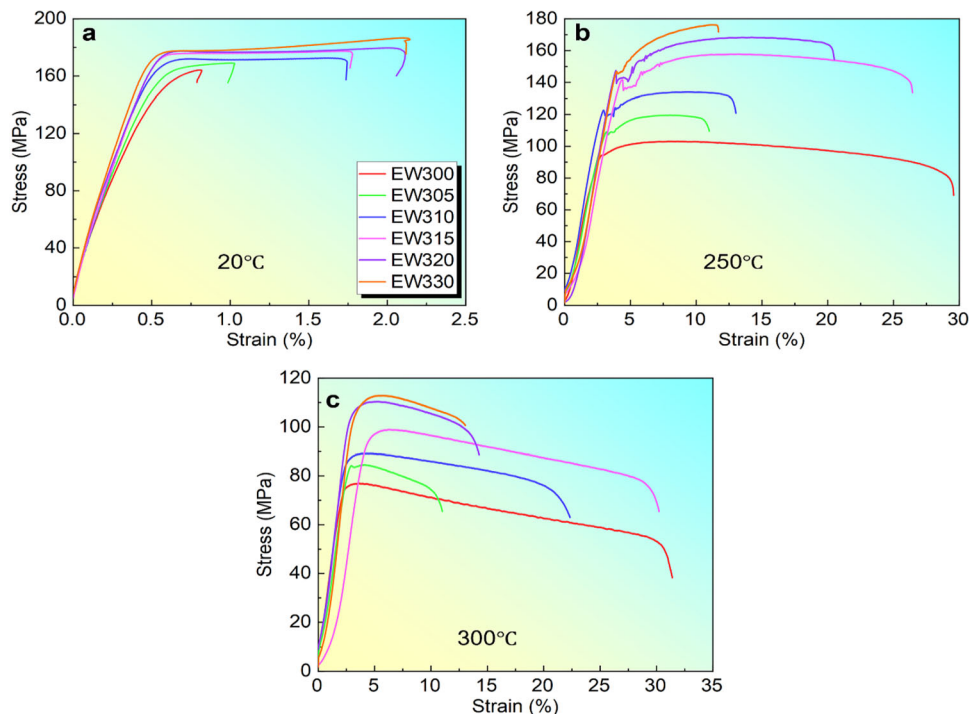


Figure 8. Tensile test curves of as-cast HPDC EW300, EW305, EW310, EW315, EW320, and EW330 alloys at (a) 20 °C, (b) 250 °C, and (c) 300 °C, respectively.

Tensile Properties at RT and HTs

Figures 8 and 9 depict the tensile test curves and tensile performance of the HPDC EW300, EW305, EW310, EW315, EW320, and EW330 alloys at RT and HTs. The yield strength (YS) and elongation (El) of the alloys increase proportionally with the increment of Y added at

RT. Compared with EW300 alloy, the YS of EW330 alloy at RT increases by 22.2%, and the El increases from 0.8 to 2.1%. Additionally, the addition of Y increases the strength of the alloy at HT. The YS of EW330 increases by 71.3% at 250 °C and by 44.9% at 300 °C, in comparison to the EW300. Therefore, the YS at HT can be enhanced effectively with Y addition. In addition, incorporating Y

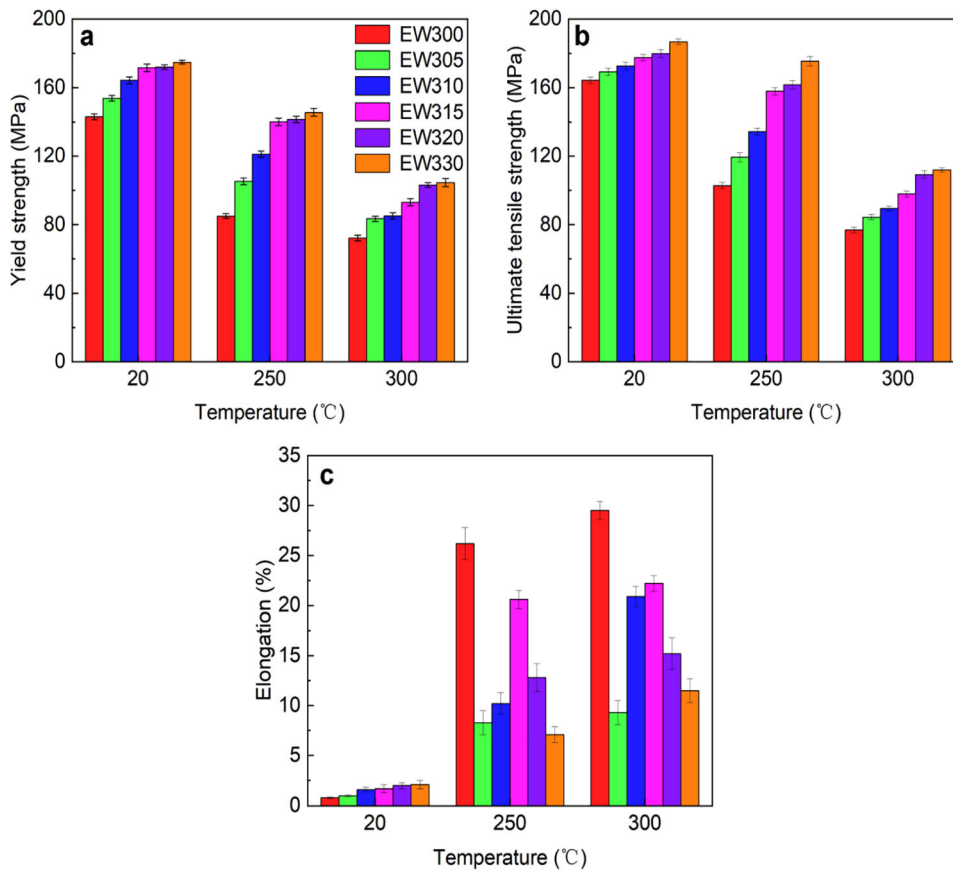


Figure 9. Tensile performance of HPDC EW300, EW305, EW310, EW315, EW320, and EW330 alloys at RT (20 °C) and HTs (250 °C and 300 °C) under as-cast condition. (a) YS, (b) UTS, and (c) EI.

Table 2. Tested Tensile Properties of HPDC EW300, EW305, EW310, EW315, EW320, and EW330 Alloys at RT and HTs

Alloy	20 °C			250 °C			300 °C		
	YS (MPa)	UTS (MPa)	EI (%)	YS (MPa)	UTS (MPa)	EI (%)	YS (MPa)	UTS (MPa)	EI (%)
EW300	143.1 ± 2	164.3 ± 2	0.8 ± 0.1	85.0 ± 1	102.9 ± 2	26.2 ± 1.6	72.2 ± 2	76.9 ± 2	29.5 ± 0.9
EW305	153.9 ± 2	169.1 ± 2	1.0 ± 0.1	105.3 ± 2	119.4 ± 3	8.3 ± 1.2	83.4 ± 2	84.4 ± 2	9.3 ± 1.2
EW310	164.2 ± 2	172.6 ± 2	1.6 ± 0.2	121.2 ± 2	134.4 ± 2	10.2 ± 1.1	85.1 ± 2	89.5 ± 1	20.9 ± 1.0
EW315	171.6 ± 2	177.5 ± 2	1.7 ± 0.4	140.1 ± 2	157.8 ± 2	20.6 ± 0.9	93.1 ± 2	97.9 ± 2	22.2 ± 0.8
EW320	171.9 ± 1	179.8 ± 2	2.0 ± 0.3	141.5 ± 2	161.6 ± 2	12.8 ± 1.4	103.2 ± 1	109.3 ± 2	15.2 ± 1.6
EW330	174.8 ± 1	186.7 ± 2	2.1 ± 0.4	145.6 ± 2	175.4 ± 3	7.1 ± 0.8	104.6 ± 2	112.1 ± 1	11.5 ± 1.2

decreases the elongation of the alloy at HTs compared to Y-free alloys. Table 2 displays the mean and standard deviation of tensile properties of as-cast HPDC EW300, EW305, EW310, EW315, EW320, and EW330 alloys.

Fractured Surface

Figure 10 shows the fractured surfaces of HPDC EW300, EW305, EW310, EW315, EW320, and EW330 alloys at RT. Figure 10a indicated that distinct river-like cleavage

planes were present at the fracture of the EW300 alloy. Figure 10b–f indicated that with the increasing addition of Y, the cleavage planes gradually decreased, and the ductile characteristics around the cleavage planes increased, which agreed with the ductility increase at RT (Figure 8a). In addition, Figure 10g–l shows the presence of fine transgranular cracks in all alloys. Therefore, the mechanisms for fracture of HPDC EW300, EW305, EW310, EW315, EW320, and EW330 alloys were a mixture of quasi-cleavage and ductile fracture.

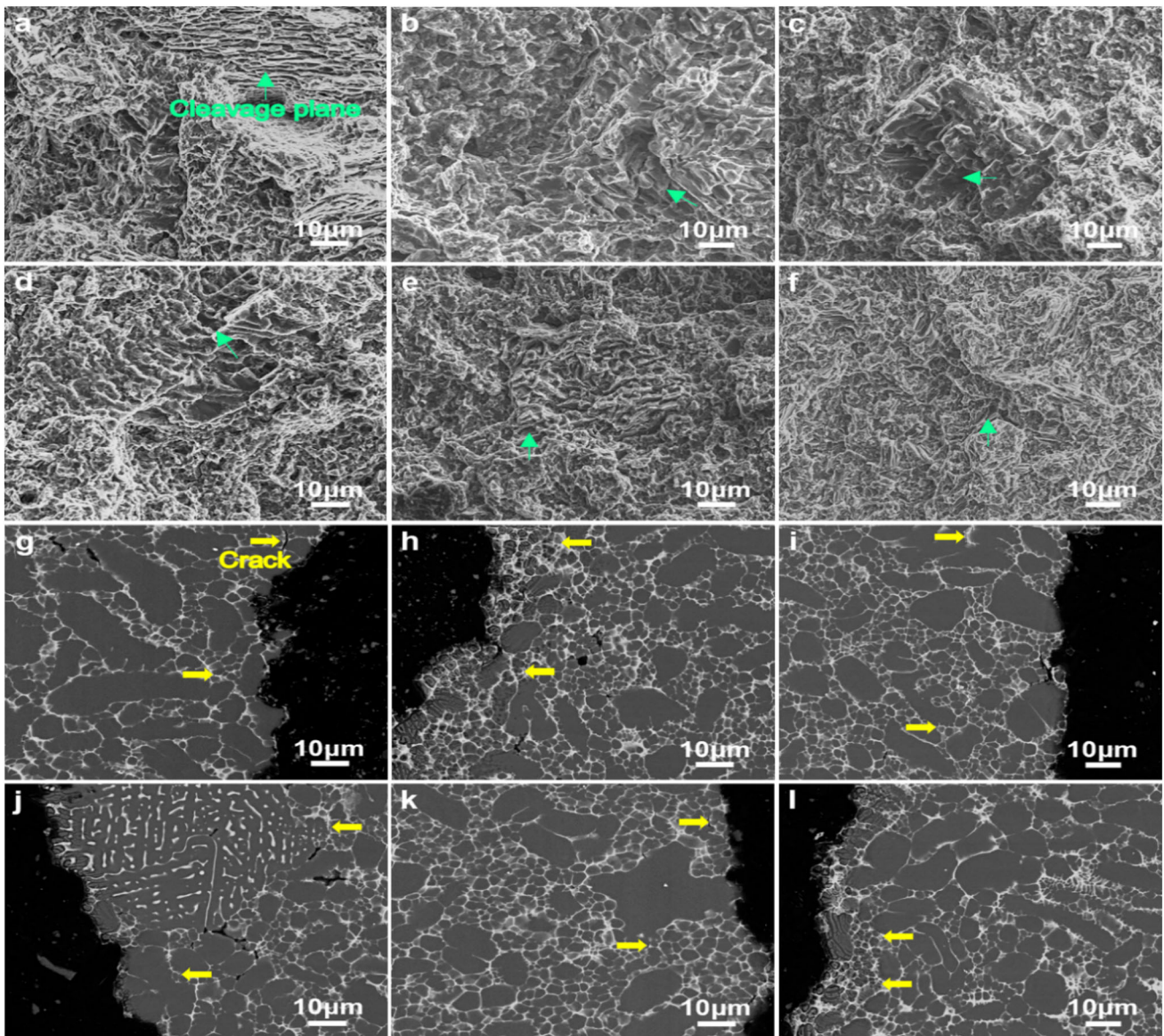


Figure 10. Cross-sectioned and longitudinal-sectioned SEM fracture micrographs of HPDC (a, g) EW300, (b, h) EW305, (c, i) EW310, (d, j) EW315, (e, k) EW320, and (f, l) EW330 alloys at RT.

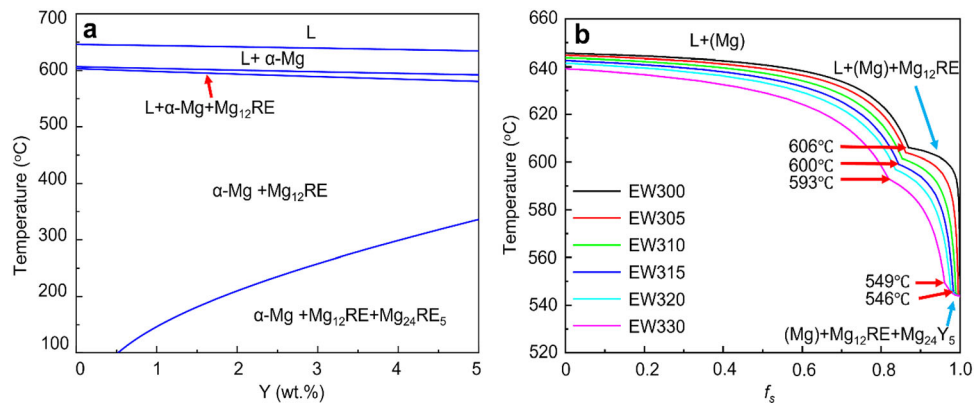


Figure 11. Non-equilibrium Scheil calculated phase diagram and solidification curves with the Pandat CALPHAD software. (a) Calculated phase diagram of the EW alloys; (b) calculated solidification curves of the EW300, EW305, EW310, EW315, EW320, and EW330 alloys.

Discussion

Microstructural Evolution

The evolution of the microstructure can be demonstrated by the solidification procedure. During solidification, the eutectic reaction of the Mg–Y binary alloy occurs at Mg–3.75 at% Y (Mg–12.0 wt% Y).³⁶ Consequently, the investigated alloys should be hypo-eutectic in this study. Figure 11a shows the phase diagrams of the EW alloys calculated by the Pandat CALPHAD software. The phase diagram for the Y-modified alloy reveals the presence of three distinct phases: α -Mg, Mg₁₂RE, and Mg₂₄RE₅. According to the analysis in Figure 11a, the Mg₂₄RE₅ phase begins to form at about 0.5% Y addition agrees with the results in Figure 6. Calculated solidification curves of HPDC EW300, EW305, EW310, EW315, EW320, and EW330 alloys are shown in Figure 11b, as determined by the Pandat CALPHAD software. With the increasing addition of Y, liquidus temperatures of the EW series alloys and the Mg₁₂RE phase formation temperature decrease. The calculated results of the Mg₁₂RE and Mg₂₄Y₅ phases are consistent with those of previous experiments.

Microstructure–Tensile–Property Relationships

As shown in Figures 8 and 9 and Table 2, increased Y addition to the EW alloys can enhance the YS at RT and HT. In terms of second phase strengthening ($\Delta\sigma_{sp}$), grain refinement strengthening ($\Delta\sigma_{gr}$), and solution strengthening ($\Delta\sigma_{ss}$), the strengthening mechanism of as-cast HPDC EW alloys can be described as follows in Eqn. 1.^{22,37,38}

$$\Delta\sigma_{EW} = \Delta\sigma_{gr} + \Delta\sigma_{ss} + \Delta\sigma_{sp} \quad \text{Eqn. 1}$$

The Hall–Petch equation can be utilised to characterise grain refinement strengthening in Eqn. 2.³⁹

$$\Delta\sigma_{gb} = Kd^{-\frac{1}{2}} \quad \text{Eqn. 2}$$

where K is the material constant and d is the mean grain size. Figure 2a–f indicates that adding Y up to 1.5% has a slight grain refinement in EW alloys. Therefore, the grain refinement effect of Y addition is calculated to be 1.2, 2.8, 4.6, 3.7, and 4.2 MPa, respectively. In the solidification process, Y segregation leads to supercooling of the solid–liquid interface components, which can promote nucleation of new grains and thus inhibit the growth of existing grains.^{6,40} Furthermore, it has been reported that the Mg₂₄Y₅ phase is assumed to promote heterogeneous nucleation during solidification and thus obtain grain refinement.^{6,40} With increased Y content, a greater growth restriction factor leads to an increased refinement effect. However, the latent heat of crystallisation released

with the formation of more Mg–RE intermetallic phases reduces the subcooling and weakens the refinement effect.⁴¹ Therefore, Y addition has a minor improvement on the tensile strength of EW alloys with grain refinement strengthening.

Following the Mg–Y, Mg–La, and Mg–Ce binary alloy phase diagram, in comparison to La (0.23%) and Ce (0.74%), the equilibrium solubility of Y (12.0%) in Mg is significantly greater.^{22,42} Therefore, the solution-strengthening mechanism is supposed to affect Y-containing Mg alloys significantly.⁴³ The Gypen and Deruyttere⁴⁴ can be used to express $\Delta\sigma_{ss}$ in Eqn. 3:

$$\Delta\sigma_{ss} = \left(\sum_i \left(k_i^{1/n} C_i \right) \right)^n \quad \text{Eqn. 3}$$

where k_i and n are material constant, C_i is the solid solution amount. According to EDS scanning results of the matrix in Supplementary Figure S2 and Table S2, the solidified Y (0.17%) is lower than solidified La (0.29%) and solidified Ce (0.27%) in the EW330 alloy. Furthermore, the solid solution content of Y in EW alloys with up to 1.5% Y was detected as almost 0. According to the report, there is an interaction between different RE elements, and adding La/Ce and Y simultaneously decreases the matrix solubility of Y.⁴⁵ Therefore, the solid solution-strengthening effect is calculated to be 2.4, 4.4, and 4.9 MPa for additions above 1.5% Y, respectively. Overall, the solid solution strengthening of Y is meaningful for additions of Y above 1.5%. However, the solid solution strengthening of Y is not significant due to the low content of dissolved Y.

Mg–RE intermetallic phase formation at GBs can impede dislocation movement, leading to second phase strengthening.⁴⁶ The second phase strengthening effect resulting from the addition of Y is 9.6, 18.3, 23.9, 22.7, and 23.1 MPa by Eqns. 1, 2, and 3, respectively. As shown in Figures 1, 2, 3 and 4, the dominant Mg₁₂RE phase and the minor Mg₂₄Y₅ and Mg₃Y phase increase with increasing Y addition in the EW alloys. These intermetallic phases can hinder dislocation movement across GBs, thus enhancing YS. The area fraction of intermetallic phases presented in Figure 3 increases significantly with the increasing Y addition, indicating that second phase strengthening is the dominant strengthening mechanism for strengthening EW alloys.

It is generally thought that the second phase at GBs can also hinder dislocation movement at HT.⁴⁷ In EW alloys, the melting point of dominant Mg₁₂RE and the minor Mg₂₄Y₅ are both relatively high, around 640 °C and 605 °C, respectively.⁴⁸ The thermally stabilised high melting point intermetallic phase contributes to the strengthening of alloys at HT. The irregular intermetallic phase Mg₃Y would decompose to Mg₂₄Y₅ and Mg₂Y at 588 K,³³ and it should be stable up to 300 °C and

contribute to the strength improvement at 250 °C and 300 °C. Therefore, the increase of the Mg₁₂RE, Mg₂₄Y₅, and Mg₃Y phases with increasing Y contributes to the increase of YS in EW alloys at HTs.

The EI of the alloy, however, shows a different trend with the addition of Y from that of the strength, decreasing, then increasing, and then decreasing. In contrast to alloys without Y additions, the thermal stable Mg–Y phases formed at the GBs in Y-containing alloys, thus hindering dislocation motion at HTs of 250 °C and 300 °C, which leads to a reduction in plasticity. For alloys with Y additions below 1.5 wt%, the grain size decreases gradually with Y addition. More refined grains introduced more GBs and more dislocation density and then improved the strength and plasticity. Thus, the EI for alloys with Y additions below 1.5 wt% shows an increasing trend at HTs. However, with Y additions higher than 1.5 wt%, the excessive RE additions make the non-uniformly distributed massive Mg–Y phases gradually coarsened, and then generates stress concentration during the plastic deformation of HT tensile, which promotes the emergence and expansion of microcavities and decreases the EI of the alloys at HTs.

Conclusions

The microstructure and tensile properties of HPDC EW alloys at RT and HTs were studied, and conclusions are summarised below:

- (1) The dominant skeleton-like phase at GBs is Mg₁₂RE. The blocky Mg₂₄Y₅ phase and the irregular Mg₃Y phase are formed with Y addition. Moreover, {011} twins were observed in the dominant Mg₁₂RE phase.
- (2) The increase in Y results in an increment of the area fraction of intermetallic phase, while it has a restricted contribution to the decrease of the mean grain size. Compared with the Y-free EW300 alloy, the area fraction of intermetallic phase in the 3% Y (EW330) alloy increases dramatically from 14.5 to 18.4%.
- (3) With the addition of Y, the YS is improved at both RT and HTs. The YS of EW330 alloy at RT and 300 °C is 174.8 MPa and 104.6 MPa, which are increased by 22.2% and 44.9%, respectively, compared to the EW300 alloy. In addition, the addition of Y causes an increase in the EI at RT.
- (4) The improvement of YS at RT is attributed to the second phase strengthening. The increase of the thermally stable Mg₁₂RE, Mg₂₄Y₅, and Mg₃Y phases contribute to the enhancement of YS at HTs. The fracture mechanism of EW alloys is a ductile and quasi-cleavage fracture blend at RT.

Acknowledgements

This paper is an invited submission to IJMC selected from presentations at the Light Metals Technology Conference (LMT2023), held July 10 to 12, 2023, in Melbourne, Australia, based upon that original presentation. The financial support from Innovate UK (Project reference: 10004694) is gratefully acknowledged.

Author Contributions

L. Feng contributed to the experimental conduction, data analysis, results analysis, and manuscript preparation. X. Dong was involved in the supervision, conception, experimental design, results analysis, manuscript revision and proof. Q. Cai assisted in the phase identification and data analysis. S. Ji contributed to the fund acquisition and manuscript proof.

Conflict of interest The authors declare that they have no known competing financial interests or personal relationships that could have appeared to influence the work reported in this paper.

Open Access

This article is licensed under a Creative Commons Attribution 4.0 International License, which permits use, sharing, adaptation, distribution and reproduction in any medium or format, as long as you give appropriate credit to the original author(s) and the source, provide a link to the Creative Commons licence, and indicate if changes were made. The images or other third party material in this article are included in the article's Creative Commons licence, unless indicated otherwise in a credit line to the material. If material is not included in the article's Creative Commons licence and your intended use is not permitted by statutory regulation or exceeds the permitted use, you will need to obtain permission directly from the copyright holder. To view a copy of this licence, visit <http://creativecommons.org/licenses/by/4.0/>.

REFERENCES

1. J.F. Song, J. Chen, X.M. Xiong, X.D. Peng, D.L. Chen, F.S. Pan, Research advances of magnesium and magnesium alloys worldwide in 2021. *J. Magnes. Alloys* **10**, 863–898 (2022). <https://doi.org/10.1016/j.jma.2022.04.001>
2. H. Ning, Y. Yu, B. Gao, L. Xiao, L. Wen, Z. Yan, L. Li, X. Chen, Grain refinement and aging hardening of the Mg-10Gd-3Y-2Ag-0.4Zr alloy produced by a two-step forming process. *Materials* **11**(5), 757 (2018). <https://doi.org/10.3390/ma11050757>
3. W. Zhang, J. Xu, Advanced lightweight materials for automobiles: a review. *Mater. Des.* **221**, 110994 (2022). <https://doi.org/10.1016/j.matdes.2022.110994>

4. S.V.S. Prasad, S.B. Prasad, K. Verma, R.K. Mishra, V. Kumar, S. Singh, The role and significance of magnesium in modern day research-a review. *J. Magnes. Alloys* **10**(1), 1–61 (2021). <https://doi.org/10.1016/j.jma.2021.05.012>
5. S. Gavras, S.M. Zhu, J.F. Nie, M.A. Gibson, M.A. Easton, On the microstructural factors affecting creep resistance of die-cast Mg–La-rare earth (Nd, Y or Gd) alloys. *Mater. Sci. Eng. A* **675**, 65–75 (2016). <https://doi.org/10.1016/j.msea.2016.08.046>
6. D.H. Stjohn, M.A. Easton, M. Qian, J.A. Taylor, Grain refinement of magnesium alloys: a review of recent research, theoretical developments, and their application. *Metall. Mater. Trans. A* **44**, 2935–2949 (2013). <https://doi.org/10.1007/s11661-012-1513-x>
7. H.Y. Wang, Z.P. Yu, L. Zhang, C.G. Liu, M. Zha, C. Wang, Q.C. Jiang, Achieving high strength and high ductility in magnesium alloy using hard-plate rolling (HPR) process. *Sci. Rep.* **5**, 17100 (2015). <https://doi.org/10.1038/srep17100>
8. W.L. Xiao, M.A. Easton, S.M. Zhu, M.S. Dargusch, M.A. Gibson, S.S. Jia, J.F. Nie, Casting defects and mechanical properties of high pressure die cast Mg–Zn–Al–RE alloys. *Adv. Eng. Mater.* **14**(1–2), 68–76 (2012). <https://doi.org/10.1002/adem.201100149>
9. B. Hu, W.J. Zhu, Z.X. Li, S.B. Lee, D.J. Li, X.Q. Zeng, Y.S. Choi, Effects of Ce content on the modification of Mg₂Si phase in Mg–5Al–2Si alloy. *J. Magnes. Alloys* **11**(7), 2299–2311 (2021). <https://doi.org/10.1016/j.jma.2021.08.031>
10. A. Suzuki, N. Saddock, J. Jones, T. Pollock, Structure and transition of eutectic (Mg, Al)₂Ca Laves phase in a die-cast Mg–Al–Ca base alloy. *Scr. Mater.* **51**(10), 1005–1010 (2004). <https://doi.org/10.1016/j.scriptamat.2004.07.011>
11. Z.T. Li, X.G. Qiao, C. Xu, S. Kamado, M.Y. Zheng, A.A. Luo, Ultrahigh strength Mg–Al–Ca–Mn extrusion alloys with various aluminum contents. *J. Alloys Compd.* **792**, 130–141 (2019). <https://doi.org/10.1016/j.jallcom.2019.03.319>
12. X.X. Dong, L.Y. Feng, S.H. Wang, F. Wang, R. Ghasemi, G. Ji, E.A. Nyberg, S.X. Ji, A quantitative strategy for achieving the high thermal conductivity of die-cast Mg–Al-based alloys. *Materialia* **22**, 101426 (2022). <https://doi.org/10.1016/j.mtla.2022.101426>
13. S.M. Zhu, T.B. Abbott, J.F. Nie, H.Q. Ang, D. Qiu, K. Nogita, M.A. Easton, Re-evaluation of the mechanical properties and creep resistance of commercial magnesium die-casting alloy AE44. *J. Magnes. Alloys* **9**(5), 1537–1545 (2021). <https://doi.org/10.1016/j.jma.2021.04.016>
14. X.X. Dong, L.Y. Feng, S.H. Wang, G. Ji, A. Addad, H.L. Yang, E.A. Nyberg, S.X. Ji, On the exceptional creep resistance in a die-cast Gd-containing Mg alloy with Al addition. *Acta Mater.* **232**, 117957 (2022). <https://doi.org/10.1016/j.actamat.2022.117957>
15. Y.H. Kang, Z.H. Huang, S.C. Wang, H. Yan, R.S. Chen, J.C. Huang, Effect of pre-deformation on microstructure and mechanical properties of WE43 magnesium alloy II: aging at 250 and 300 °C. *J. Magnes. Alloys* **8**(1), 103–110 (2020). <https://doi.org/10.1016/j.jma.2019.11.012>
16. L.R. Xiao, Y. Cao, S. Li, H. Zhou, X.L. Ma, L. Mao, X.C. Sha, Q.D. Wang, Y.T. Zhu, X.D. Han, The formation mechanism of a novel interfacial phase with high thermal stability in a Mg–Gd–Y–Ag–Zr alloy. *Acta Mater.* **162**, 214–225 (2019). <https://doi.org/10.1016/j.actamat.2018.10.005>
17. J.H. Zhang, M.L. Zhang, J. Meng, R.Z. Wu, D.X. Tang, Microstructures and mechanical properties of heat-resistant high-pressure die-cast Mg–4Al–xLa–0.3Mn (x = 1, 2, 4, 6) alloys. *Mater. Sci. Eng. A* **527**(10–11), 2527–2537 (2010). <https://doi.org/10.1016/j.msea.2009.12.048>
18. T. Rzychoń, A. Kiełbus, L. Lityńska-Dobrzyńska, Microstructure, microstructural stability and mechanical properties of sand-cast Mg–4Al–4RE alloy. *Mater Charact* **83**, 21–34 (2013). <https://doi.org/10.1016/j.matchar.2013.06.001>
19. G.H. Wu, C.L. Wang, M. Sun, W.J. Ding, Recent developments and applications on high-performance cast magnesium rare-earth alloys. *J. Magnes. Alloys* **9**(1), 1–20 (2020). <https://doi.org/10.1016/j.jma.2020.06.021>
20. X.X. Dong, L.Y. Feng, S.H. Wang, E.A. Nyberg, S.X. Ji, A new die-cast magnesium alloy for applications at higher elevated temperatures of 200–300 °C. *J. Magnes. Alloys* **9**(1), 90–101 (2021). <https://doi.org/10.1016/j.jma.2020.09.012>
21. M.A. Easton, S.M. Zhu, T.B. Abbott, M. Dargusch, M. Murray, G. Savage, N. Hort, M.A. Gibson, Evaluation of magnesium die-casting alloys for elevated temperature applications: castability. *Adv. Eng. Mater.* **18**, 953–962 (2016). <https://doi.org/10.1002/adem.201500407>
22. L.Y. Feng, X.X. Dong, Q. Cai, B. Wang, S.X. Ji, Effect of Gd on the microstructure and mechanical properties of high-pressure die-cast Mg–La–Ce alloys at ambient and elevated temperatures. *J. Alloys Compd.* **923**, 166364 (2022). <https://doi.org/10.1016/j.jallcom.2022.166364>
23. L.Y. Feng, X.X. Dong, Q. Cai, B. Wang, S.X. Ji, Effect of Nd on the microstructure and mechanical properties of Mg–La–Ce alloys at ambient and elevated temperatures. *J. Mater. Eng. Perform.* **32**, 2598–2606 (2022). <https://doi.org/10.1007/s11665-022-06853-x>
24. X. Song, Y. Hu, K.J. Xue, Y.P. Wang, Z.J. Yan, Development of Mg–Zn–Mn–Y magnesium alloy with high thermal conductivity and compression properties via injection molding. *Inter Metalcast.* (2023). <https://doi.org/10.1007/s40962-023-01084-9>

25. H.N. Yu, S.M. Liu, L. Zhou, Z. Liu, Z.Q. Wei, H. Guo, Study on solidification behavior and hot tearing susceptibility of Mg–2xY–xNi alloys. *Inter Metalcast.* **15**, 995–1005 (2021). <https://doi.org/10.1007/s40962-020-00531-1>
26. J. Wang, J. Meng, D.P. Zhang, D.X. Tang, Effect of Y for enhanced age hardening response and mechanical properties of Mg–Gd–Y–Zr alloys. *Mater. Sci. Eng. A* **456**(1–2), 78–84 (2007). <https://doi.org/10.1016/j.msea.2006.11.096>
27. A. Wu, C. Xia, J. Wang, Distribution, evolution and the effects of rare earths Ce and Y on the mechanical properties of ZK60 alloys. *Int. J. Miner. Metall. Mater.* **13**, 424–428 (2006). [https://doi.org/10.1016/S1005-8850\(06\)60086-8](https://doi.org/10.1016/S1005-8850(06)60086-8)
28. S. Gavras, M.A. Easton, M.A. Gibson, S.M. Zhu, J.F. Nie, Microstructure and property evaluation of high-pressure die-cast Mg–La–rare earth (Nd, Y or Gd) alloys. *J. Alloys Compd.* **597**, 21–29 (2014). <https://doi.org/10.1016/j.jallcom.2014.01.204>
29. J. Gröbner, M. Hampl, R. Schmid-Fetzer, M.A. Easton, S.M. Zhu, M.A. Gibson, J.F. Nie, Phase analysis of Mg–La–Nd and Mg–La–Ce alloys. *Intermetallics* **28**, 92–101 (2012). <https://doi.org/10.1016/j.intermet.2012.04.012>
30. X.R. Hua, Q. Yang, D.D. Zhang, F.Z. Meng, C. Chen, Z.H. You, J.H. Zhang, S.H. Lv, J. Meng, Microstructures and mechanical properties of a newly developed high-pressure die casting Mg–Zn–RE alloy. *J. Mater. Sci. Technol.* **53**, 174–184 (2020). <https://doi.org/10.1016/j.jmst.2020.04.030>
31. M. Suzuki, T. Kimura, J. Koike, K. Maruyama, Strengthening effect of Zn in heat resistant Mg–Y–Zn solid solution alloys. *Scr. Mater.* **48**(8), 997–1002 (2003). [https://doi.org/10.1016/s1359-6462\(02\)00590-0](https://doi.org/10.1016/s1359-6462(02)00590-0)
32. M.Q. Zhang, J.H. Zhang, R.Z. Wu, H.W. Cui, E.T. Zhao, S.J. Liu, P.F. Qin, Q. Ji, The effect of Y/Er and Zn addition on the microstructure and mechanical properties of Mg–11Li alloy. *Materials* **12**(19), 3066 (2019). <https://doi.org/10.3390/ma12193066>
33. S. Burapornpong, S. Tsuchiya, T. Kimura, A. Kamegawa, High-pressure synthesis of a novel compound in Mg–Y system. *J. Alloys Compd.* **850**, 156754 (2021). <https://doi.org/10.1016/j.jallcom.2020.156754>
34. T.H. Le, Q. Wei, J.H. Wang, P.P. Jin, M.R. Chen, J.X. Ma, Effect of different casting techniques on the microstructure and mechanical properties of AE44–2 magnesium alloy. *Mater. Res. Express* **7**, 116513 (2020). <https://doi.org/10.1088/2053-1591/abc721>
35. P.F. Qin, Q. Yang, Y.Y. He, J.H. Zhang, J.S. Xie, X.R. Hua, K. Guan, J. Meng, Microstructure and mechanical properties of high-strength high-pressure die-cast Mg–4Al–3La–1Ca–0.3Mn alloy. *Rare Met.* **40**, 2956–2963 (2021). <https://doi.org/10.1007/s12598-020-01661-5>
36. A.R. Mirak, C.J. Davidson, J.A. Taylor, Study on the early surface films formed on Mg–Y molten alloy in different atmospheres. *J. Magnes. Alloys* **3**(3), 173–179 (2015). <https://doi.org/10.1016/j.jma.2015.06.003>
37. X.X. Dong, H. Youssef, X.Z. Zhu, Y.J. Zhang, S.H. Wang, S.X. Ji, High as-cast strength die-cast AlSi9–Cu2Mg alloy prepared by nanoparticle strengthening with industrially acceptable ductility. *J. Alloys Compd.* **852**, 156873 (2021). <https://doi.org/10.1016/j.jallcom.2020.156873>
38. J. Rong, J.N. Zhu, W.L. Xiao, X.Q. Zhao, C.L. Ma, A high pressure die cast magnesium alloy with superior thermal conductivity and high strength. *Intermetallics* **139**, 107350 (2021). <https://doi.org/10.1016/j.intermet.2021.107350>
39. Y. Fang, Z. Yu, S. Yuan, S. Zhang, Y. Zhang, B. Zhang, K. Wang, Q. Wei, W. Lu, X. Ma, Microstructure and enhanced mechanical properties of Mg–3Sn alloy with Mn addition. *Mater. Res. Express* **9**(9), 096514 (2022). <https://doi.org/10.1088/2053-1591/ac911a>
40. Y. Zeng, B. Jiang, M.X. Zhang, H.M. Yin, R.H. Li, F.S. Pan, Effect of Mg24Y5 intermetallic particles on grain refinement of Mg–9Li alloy. *Intermetallics* **45**, 18–23 (2014). <https://doi.org/10.1016/j.intermet.2013.09.005>
41. J.C. Dai, M. Easton, S.M. Zhu, G.H. Wu, W.J. Ding, Grain refinement of Mg–10Gd alloy by Al additions. *J. Mater. Res.* **27**, 2790–2797 (2012). <https://doi.org/10.1557/jmr.2012.313>
42. J.F. Nie, Precipitation and hardening in magnesium alloys. *Metall. Mater. Trans. A* **43**, 3891–3939 (2012). <https://doi.org/10.1007/s11661-012-1217-2>
43. L. Gao, R.S. Chen, E.H. Han, Solid solution strengthening behaviors in binary Mg–Y single phase alloys. *J. Alloys Compd.* **472**(1–2), 234–240 (2009). <https://doi.org/10.1016/j.jallcom.2008.04.049>
44. L.A. Gypen, A. Deruyttere, Multi-component solid solution hardening. *J. Mater. Sci.* **12**, 1034–1038 (1977). <https://doi.org/10.1007/BF00540988>
45. L.L. Rokhlin, E.A. Lukyanova, T.V. Dobatkina, I.G. Korolkova, Peculiarities of the physico-chemical interaction in ternary systems of magnesium with two rare-earth metals of different subgroups. *Chem. Met. Alloys* **7**, 32–36 (2014). <https://doi.org/10.30970/cma7.0265>
46. J. Rong, W.L. Xiao, Y. Fu, X.Q. Zhao, P. Yan, C.L. Ma, M. Chen, C. Huang, A high performance Mg–Al–Ca alloy processed by high pressure die casting: microstructure, mechanical properties and thermal conductivity. *Mater. Sci. Eng. A* (2022). <https://doi.org/10.1016/j.msea.2022.143500>
47. L.P. Zhong, Y.J. Wang, Y.C. Dou, On the improved tensile strength and ductility of Mg–Sn–Zn–Mn alloy processed by aging prior to extrusion. *J. Magnes.*

Alloys **7**(4), 637–647 (2019). <https://doi.org/10.1016/j.jma.2019.07.007>

48. J.S. Xie, J.H. Zhang, Z.H. You, S.J. Liu, K. Guan, R.Z. Wu, J. Wang, J. Feng, Towards developing Mg alloys with simultaneously improved strength and corrosion resistance via RE alloying. *J. Magnes.*

Alloys **9**(1), 41–56 (2021). <https://doi.org/10.1016/j.jma.2020.08.016>

Publisher's Note Springer Nature remains neutral with regard to jurisdictional claims in published maps and institutional affiliations.